Article

Effect of LiCl Electrolyte Concentration on Energy Storage of Supercapacitor with Multilayered $Ti_3C_2T_x$ MXene Electrodes Synthesized by Hydrothermal Etching

Alexey Tsyganov [1,*], Alexander Shindrov [2], Maria Vikulova [1], Denis Zheleznov [1], Alexander Gorokhovsky [1] and Nikolay Gorshkov [1,*]

[1] Department of Chemistry and Technology of Materials, Yuri Gagarin State Technical University of Saratov, 77 Polytecnicheskaya Street, 410054 Saratov, Russia
[2] Institute of Solid State Chemistry and Mechanochemistry, Siberian Branch of the Russian Academy of Sciences, 18 Kutateladze, 630128 Novosibirsk, Russia
[*] Correspondence: tsyganov.a.93@mail.ru (A.T.); gorshkov.sstu@gmail.com (N.G.)

Abstract: The development of new electrode materials for electrochemical systems for various purposes is a significant and in-demand task of scientific research. Layered transition metal carbides and nitrides, known as MXenes, show great potential for use as electrodes in electrochemical energy storage devices operating in aqueous electrolytes. In this work, a multilayer $Ti_3C_2T_x$ MXene was obtained from a Ti_3AlC_2 precursor and studied as the electrode material of a symmetrical supercapacitor with an aqueous LiCl electrolyte. The formation of the MXene structure was confirmed by the data from X-ray phase analysis and scanning electron microscopy. The X-ray diffraction pattern showed the disappearance of the main reflections related to the Ti_3AlC_2 phase and the shift of the reflection peak (002) from 9.4° to 6.7°, which indicated successful etching of the Al layers from the Ti_3AlC_2 precursor. At electrolyte concentrations of 1, 5, 10, and 20 M, the supercapacitors demonstrated high specific capacitances of 105, 120, 126, and 151 $F \cdot g^{-1}$ at a scan rate of 5 $mV \cdot s^{-1}$. In addition, an increase in the LiCl concentration contributed to the expansion of the potential window from 0.7 to 1 V. It was shown that the contribution of the surface capacitance to the total capacitance of the electrode is about 40% and depends little on the scan rate. In addition, the symmetrical supercapacitor with 5 M electrolyte showed good cyclic stability with capacitance retention of 88% over 10,000 cycles. The parameters of the main components of the physical processes of supercapacitors based on $Ti_3C_2T_x$ were determined by the method of impedance spectroscopy.

Keywords: supercapacitor; MXene; energy storage; molten salt; hydrothermal etching; capacity

1. Introduction

An important task of the modern scientific community is the development of new, highly efficient energy storage and conversion systems due to the rapid development of electronic technology and the growing need for energy storage. Among such energy storage devices, one can note lithium-ion batteries [1,2], lithium-selenium batteries [3], post-lithium and sodium-ion batteries [4], zinc-ion [5] and zinc-air batteries [6], as well as ammonium-ion batteries [7]. Among them, lithium-ion batteries clearly occupy a leading position. However, lithium-ion batteries have a slow energy supply or absorption, which limits their use in applications that require faster and more powerful energy storage systems. Supercapacitors (SCs) or ultracapacitors can handle this task [8–13]. These devices are able to charge in seconds and quickly discharge. These devices are inferior in terms of specific energy (about 5 $Wh \cdot kg^{-1}$), but the value of specific power transmitted in a few seconds is much higher (10 $kW \cdot kg^{-1}$). SCs play an important role in uninterruptible power supply and load-balancing applications. Sharing batteries and SCs allows for the creation of hybrid systems that can store more energy and release or store it in a shorter time [14].

Although SCs have been used in the electronics industry for decades, they still need to be improved. Depending on the charge storage mechanism, SCs can be divided into electrical double-layer capacitors and pseudocapacitors. In the first case, the accumulation of energy occurs as a result of the separation of charges at the interface between the electrolyte and the electrode. In the case of pseudocapacitors for energy storage, the following reactions take place: (1) intercalation of electrolyte ions; (2) redox reactions, which result in charge accumulation at the electrode/electrolyte interface; (3) low-potential deposition, in which a charge is built up by depositing ions at a metal/electrolyte interface that is negative with respect to their redox potential [15–17]. The design of SCs consists of electrodes, electrolytes, and ion-permeable membranes. Both electrode materials and electrolytes play a key role in the energy storage characteristics of SCs. Therefore, when developing SCs, it is necessary to ensure the required characteristics of the electrode material and electrolyte.

Electrode materials for modern SCs should have a number of properties such as high capacitive characteristics, high electrical conductivity, high chemical and thermal stability, surface wettability, etc. Therefore, carbon materials, conductive polymers, oxides, and sulfides of transition metals are widely studied as electrode materials [18–23]. However, most of them have low actual capacitance, low cycle stability, limited conductivity, or short life, which limits their use in modern electronic devices. More promising electrode materials can be 2d materials of the MXene group. MXene are defined by the general formula $M_{n+1}X_nT_x$ and are a relatively new group of early transition metal carbides, nitrides, and carbonitrides obtained by selective etching of element A from structures of $M_{n+1}AX_n$ phases, where M is a transition metal (Ti, Zr, V, Nb, Mo, etc.), A is an element IIIA or IVA (Al, Si, Ga, In, etc.), X is carbon and/or nitrogen, and T_x are surface functional groups (–O, –F, –OH, –Cl). MXenes have a number of unique physical and chemical properties due to which they find applications in various fields such as catalysis, electromagnetic absorption, electronics, sensors, optoelectronics, and many others [24–30]. The unique properties such as intercalation, high electrical conductivity, hydrophilicity, and surface redox reactions of MXenes make them promising candidates as high-capacity energy storage electrode materials [31–35]. Among the many different types of MXene, $Ti_3C_2T_x$ is the most widely studied. This is primarily due to its availability and a number of physicochemical properties such as high volumetric specific capacitance, high current densities, and the ability to intercalate various metal cations.

For the manufacture of SCs electrodes from MXenes, macrostructures such as films and aerogels are usually used [36–39]. However, the fabrication of such macrostructures is extremely energy intensive and economically disadvantageous. A more efficient method of obtaining electrodes is blade coating, since this method is feasible using available modern industrial equipment and processing technology, which ensures low costs and high efficiency of their production. In addition, an important problem in obtaining MXenes is their lamination into individual nanosheets. In order to laminate multilayer accordion-like MXenes, additional intercalation of TBAOH, TMAOH, or DMSO molecules into the interlayer space of the MXene, and then long-term ultrasonic treatment, is usually required. And even when using these procedures, the yield of single-layer MXene is about 40%. Although laminated MXenes exhibit higher specific electrochemical capacitance, direct use of multilayer MXenes is a simpler and more cost-effective approach.

The second important component of SCs is the electrolyte. SCs can operate both on aqueous electrolytes and on the basis of organic and ionic electrolytes. However, the use of organic electrolytes makes it possible to obtain a wider potential window of 3–4 V compared to aqueous 0.8–1.2 V, which leads to a higher energy density. Despite this, the development of high-performance SCs powered by aqueous electrolytes is an extremely important task since this significantly reduces safety requirements and costs. It is known that $Ti_3C_2T_x$ MXene exhibits the best energy storage efficiency in sulfuric acid solutions due to very fast redox reactions between H^+ ions and MXenes [40,41]. However, compared to acidic or alkaline electrolytes, neutral electrolytes are safer and allow a larger potential window to be achieved by suppressing oxygen and hydrogen evolution. Compared to

sulfuric acid, LiCl aqueous solution is one of the most common electrolytes, which is a safe neutral salt with high solubility.

For the first time, in this work, multilayer MXenes are studied as an active component of the electrode material of a symmetrical supercapacitor using an aqueous solution as an electrolyte. The aim of this study is to determine the effect of LiCl concentration in the electrolyte of a symmetrical SC with electrodes based on multilayer $Ti_3C_2T_x$ MXene deposited by the doctor-blade method.

2. Materials and Methods

2.1. Synthesis of Multilayered $Ti_3C_2T_x$ MXene

For the synthesis of Ti_3AlC_2 MAX phase powder, elemental powders of titanium carbide (TiC, 0.8–1.5 μm, 99.9%, Mreda, Beijing, China), titanium (Ti, PTM-1, 99%, Polema, Tula, Russia), aluminum (Al, PA 4, 98%, Nizhny Novgorod, Russia), potassium, and sodium chlorides were used. Ti_3AlC_2 MAX phase powder was obtained using molten salt shielded synthesis. This synthesis method was chosen because of the higher diffusion rate and property of non-oxide materials' oxidation inhibition. For synthesis, TiC, Ti, and Al powders were ground in a Frisch Pulverisette 6 planetary mill for 1 h using ZrO_2 balls 2 mm in diameter. The stoichiometric molar ratio TiC:Ti:Al was 2:1:1.4 due to the high volatilization of aluminum. Cylindrical granules 12 mm in diameter and 15 mm in height were obtained from the resulting reaction mixture by uniaxial pressing. The granules were immersed in an Al_2O_3 crucible preheated to 800 °C containing the eutectic composition of the NaCl:KCl salt flux with a molar ratio of 0.506:0.494. Then, the crucible was covered with a lid and kept in a furnace at 1250 °C for 3 h in a natural air atmosphere. After natural cooling, the mixture was washed with distilled water to remove sodium and potassium chlorides, and then washed in HCl solution for 18 h to remove possible intermetallic phases. For washing 1 g of the MAX phase, 7.5 mL of HCl (11.8 M) and 2.5 mL of H_2O were used. Then, the powder was washed on a vacuum filter and dried at 60 °C. It should be noted that the resulting Ti_3AlC_2 product was a gray powder without the use of additional grinding procedures.

$Ti_3C_2T_x$ MXene multilayer materials were obtained by selective etching of an Al layer from the precursor structure of Ti_3AlC_2 MAX phase by treating it in a mixture of HCl (HCl, 11.8 M, NizhHimProm, Nizhny Novgorod, Russia) and LiF (≥98.5 wt.%, Guangfu Fine Chemical Research Institute, Tianjin, China) under hydrothermal conditions [42]. A mixture of 75 mL HCl (11.8 M), 75 mL H_2O, and 2.8 g LiF was placed in a 400 mL Teflon autoclave, and then 6 g of Ti_3AlC_2 precursor was added. The autoclave was hermetically sealed and kept in an oven at 140 °C for 24 h. It should be noted that an excess of the indicated volume of the etchant mixture in the volume of the autoclave is unacceptable for safety reasons, since the ongoing reaction is accompanied by a large release of thermal energy. After natural cooling, the resulting black dispersion was washed with distilled water on a vacuum filter until a neutral pH was established, and then dried at 60 °C for 24 h.

2.2. Materials Characterization

An ARL X'TRA diffractometer (Thermo Scientific, Ecublens, Switzerland) with Cu-Kα radiation at a wavelength of $\lambda = 0.15412$ nm and an ASPEX Explorer scanning electron microscope (ASPEX, Framingham, MA, USA) were used to study the phase composition and morphology of the multilayer $Ti_3C_2T_x$ MXene powder. To study the chemical composition by the EDX method, cylindrical granules 12 mm in diameter and 1.5 mm thick were pressed from Ti_3AlC_2 and $Ti_3C_2T_x$ powders. EDX spectra were obtained from the surface of granules with an area of 6×6 μm.

2.3. Electrochemical Testing

The SCs' electrodes were fabricated using the blade coating method. For this, a dispersion of multilayer $Ti_3C_2T_x$ MXene and carbon black (Printex RX2B) was prepared

in a 2% poly(vinylidene fluoride) solution (PVDF, Sigma Aldrich, Mw~530,000, St. Louis, MO, USA). The mass ratio of the components of the $Ti_3C_2T_x$/CB/PVDF electrode system was 8/1/1, and 1-methyl-2-pyrrolidone was used as a solvent. The coating was uniformly deposited on nickel foil 50 μm in thickness, and then dried at 80 °C under vacuum. The density of the resulting coating was 2.5 mg·cm^{-2}. Electrochemical studies of the fabricated electrodes were carried out in assembled symmetrical supercapacitors coin cell CR2032 using a P-50 PRO potentiostat (OOO, Elins, Russia) and a Z1000P impedancemeter (OOO, Elins, Russia). Aqueous solutions of lithium chloride (LiCl, 99.2%, TC 6-09-3751-838, Rushim, Moscow, Russia) with concentrations of 1, 5, 10, and 20 M were used as electrolytes. Cyclic voltammetry was used at scan rates from 1 to 100 mV·s^{-1} in a two-electrode circuit with a voltage range from 0 to 1 V. Galvanostatic charge/discharge was recorded at current densities of 0.5–5 A·g^{-1}.

The capacitance of a symmetric SC was estimated based on the results of CVs and the curves of GCDs using Equations (1) and (2), respectively:

$$C_{SC} = \frac{\int j dU}{2 \cdot \Delta U_{CV} \cdot \nu}, \text{F} \tag{1}$$

$$C_{SC} = \frac{j_{GD} \Delta t}{\Delta U_{GD}}, \text{F} \tag{2}$$

where $\int j dV$ is the integral of the current curve of the graph of the CV (mA·mV); ΔU_{CV} is the change in cell voltage CV (mV); ν is the scan rate (mV·s^{-1}); j_{GD} is the current galvanostatic discharge (mA); Δt is the discharge or charge duration (s); and ΔU_{GD} is the change in cell voltage galvanostatic discharge corrected from the ohmic drop (mV).

Thus, the specific capacitance C_m (F·g^{-1}) of a single electrode is:

$$C_m = \frac{2 \cdot C_{SC}}{0.5 \cdot m_{el}}, \text{F·g}^{-1} \tag{3}$$

where m_{el} is the total mass of MXene electrodes (g).

3. Results and Discussion

Powder diffraction patterns of the Ti_3AlC_2 MAX phase precursor and the corresponding $Ti_3C_2T_x$ MXene are shown in Figure 1. As can be seen, a pure Ti_3AlC_2 phase is formed by the processing of the TiC:Ti:Al mixture in the eutectic melt at 1250 °C. This result confirms the effectiveness of this method, since the reaction temperature and time are much lower than in solid-phase synthesis in an inert atmosphere. In addition, the absence of secondary phases of intermetallic compounds should be noted; these are probably removed during the processing of the MAX phase powder in an HCl solution. Further hydrothermal treatment of the Ti_3AlC_2 powder in an HCl/LiF mixture leads to the disappearance of most of the MAX phase diffraction peaks and the appearance of diffraction peaks at 6.7°, 13.84°, 24.8°, and 34.14° corresponding to the (002), (004), (006), and (008) planes. This indicates the transformation of the MAX phase into the corresponding Ti_3C_2 MXene [43]. In addition, during the formation of MXene, the appearance of a non-basal diffraction peak (110) is observed at an angle different from the MAX phase. It should be noted that the reflection peak (002) is significantly shifted to a smaller angle, from 9.4° to 6.7°. This indicates successful etching of the Al layers from the Ti_3AlC_2 structure, leading to the breaking of the metallic bond and successful exfoliation of the $Ti_3C_2T_x$ MXene layers. It should be noted that a strong shift of the reflection peak from the (002) plane, which characterizes an increase in the d-spacing, is associated with the intercalation of lithium ions into the MXene interlayer space.
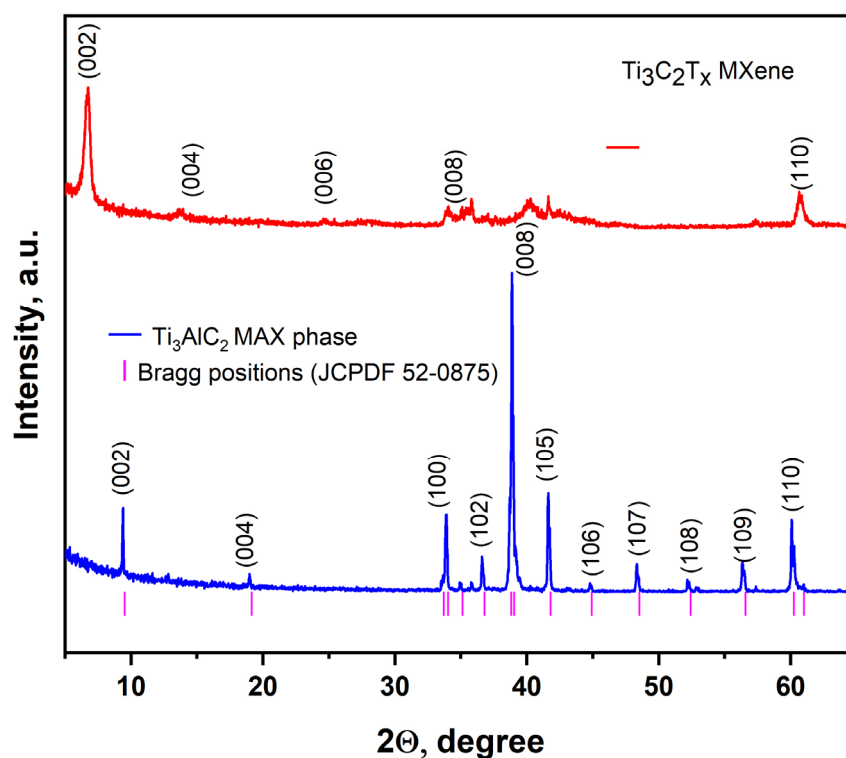
Figure 1. XRD patterns of Ti_3AlC_2 MAX phase and $Ti_3C_2T_x$ MXene powders.

The microstructure and morphology of the obtained Ti_3AlC_2 MAX phase and $Ti_3C_2T_x$ MXene powder can be observed on the SEM image in Figure 2. As can be seen, the resulting Ti_3AlC_2 MAX phase has a platelet-like morphology typical of MAX phase of layered structures. The obtained $Ti_3C_2T_x$ MXene has an accordion-like morphology formed from interconnected 2D nanolayers, which corresponds to the typical multilayer structure of MXene and confirms the successful etching of Al from the structure of the Ti_3AlC_2 MAX phase, leading to exfoliation of Ti_3C_2 MXene layers.

EDX spectra of the Ti_3AlC_2 precursor powder and the $Ti_3C_2T_x$ MXene obtained from it are shown in Figure 2c. Intense peaks of Ti (4.508 keV) and Al (1.486 keV), as well as a small presence of Cl (2.621 keV) associated with washing the sample in an HCl solution are observed on the EDX spectrum of the Ti_3AlC_2 powder. After treatment of Ti_3AlC_2 in an HCl/LiF mixture, an almost complete disappearance of the Al peak (1.486 keV) is observed, which leads to exfoliation of the Ti_3C_2 MXene layers. In addition, the presence of peaks characteristic of Cl and F, which are present in the sample in the form of surface functional groups (T_x = F, Cl), should be noted.

Cyclic voltammetry (CV) was performed to evaluate the specific capacitance. The CV curves for supercapacitors tested at scan rates from 1 to 100 $mV \cdot s^{-1}$ at LiCl electrolyte concentrations from 1 M to 20 M are shown in Figure 3. As can be seen, the CV curves show almost rectangular shapes at electrolyte concentrations up to 10 M, which indicates a capacitive charge accumulation mechanism. With an increase in LiCl concentration to 20 M, a strong deviation of the CV curves from a rectangular shape is observed, which may be associated with an increase in resistance. At the same time, an increase in the electrolyte concentration suppresses the reaction of oxygen evolution from H_2O, which, in turn, makes it possible to expand the potential window.
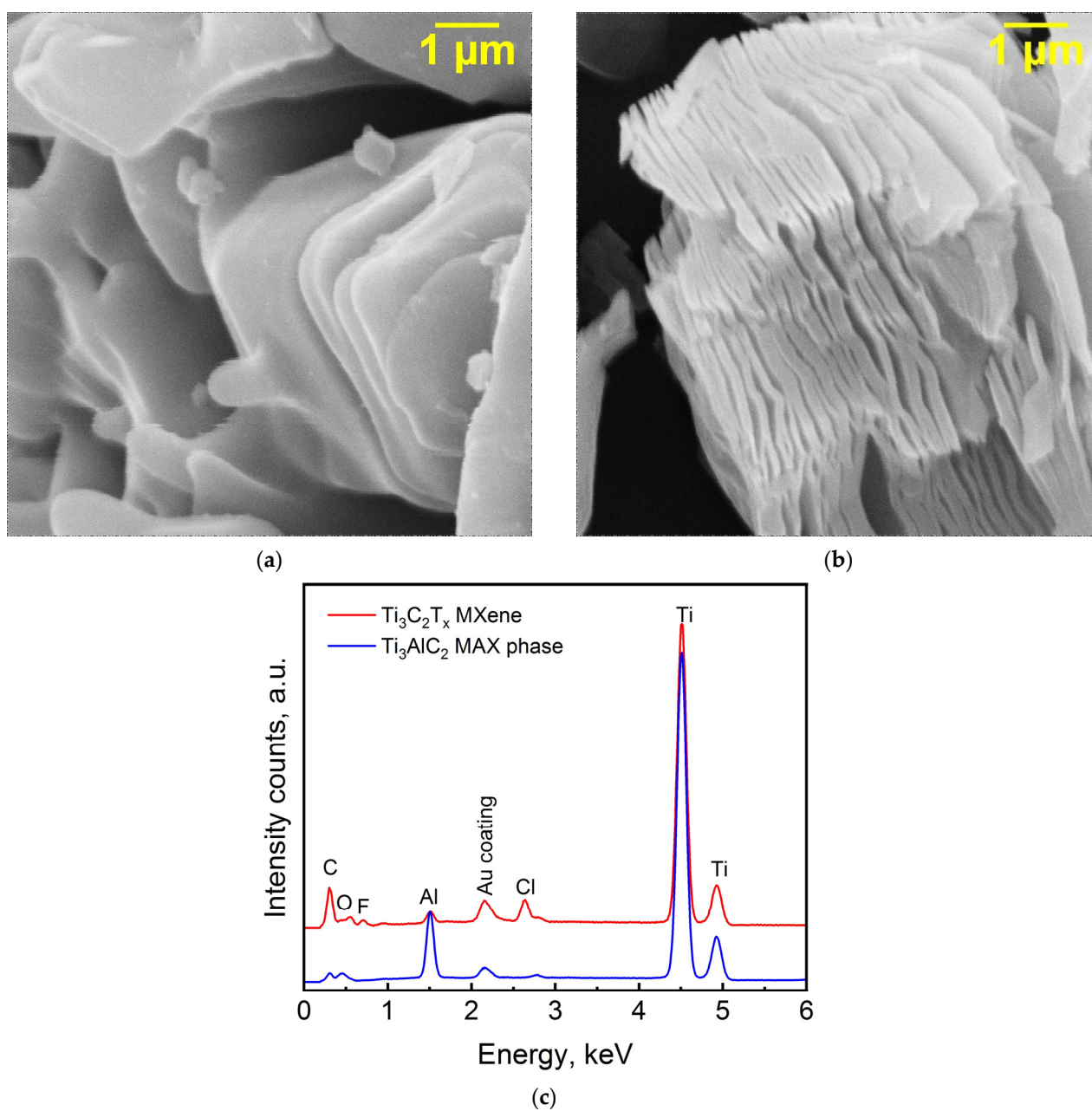
(**a**)   (**b**)

(**c**)

Figure 2. SEM images of (**a**) Ti_3AlC_2 MAX phase and (**b**) multilayer $Ti_3C_2T_x$ MXene. (**c**) EDX spectra of Ti_3AlC_2 MAX phase and $Ti_3C_2T_x$ MXene.

The dependence of the specific capacitance on the potential scan rate is shown in Figure 4a. All measurements were carried out using an aqueous LiCl electrolyte with various salt concentrations. The electrolyte concentration significantly affected the specific capacitance of SCs. At a scan rate of $5 \, mV \cdot s^{-1}$, for SCs with electrolyte concentrations of 1, 5, 10, and 20 M, the specific capacitances were 105, 120, 126, and $151 \, F \cdot g^{-1}$, respectively. In addition, it can be seen that with an increase in the potential scan rate, the specific capacitance decreases, since at a low scan rate, discharge current ions can penetrate into the layered structure of the entire electrode, which leads to maximum capacitive characteristics. However, the sample with 5 M aqueous electrolyte demonstrates the best stability with respect to scan rate, for which the specific capacitance decreases from $120 \, F \cdot g^{-1}$ to $90 \, F \cdot g^{-1}$ as the scan rate increases from 5 to $100 \, mV \cdot s^{-1}$. At the same time, the sample with 10 M electrolyte also demonstrates high stability with increasing scanning rate. In addition, for a sample with a 10 M electrolyte, the potential window is wider than for a 5 M sample,

which corresponds to its higher specific energy at a similar value of specific capacitance. The relatively high scan rate stability for samples with 5 and 10 M electrolytes can be explained by the higher electrical conductivity of the electrolytes at these concentrations, which results in rapid ion transport between the electrode and electrolyte.
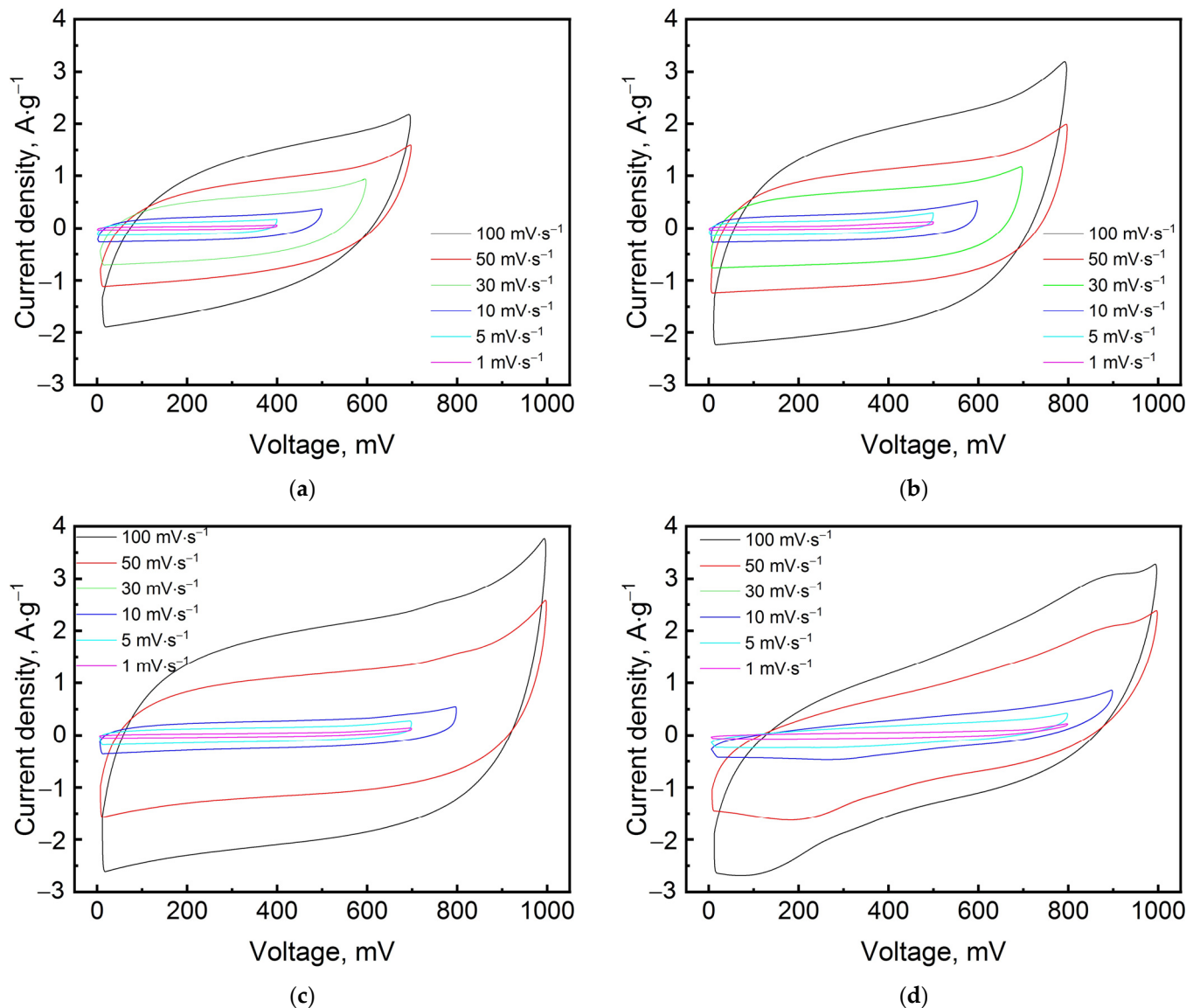

Figure 3. CV curves at different scan rates for LiCl concentrations: (**a**) 1 M, (**b**) 5 M, (**c**) 10 M, (**d**) 20 M.

It is acknowledged that two components contribute to charge accumulation [44]: (1) pseudocapacity due to the fast Faraday transfer process and non-Faraday component due to ion adsorption; (2) diffusion-controlled Faraday processes. When testing electrochemical properties using CV curves, the current i can be represented as a combination of the current generated in a diffusion driven process i_{diff} and processes dominated by surface capacitance i_{cap}, whether electric double-layer capacitors or pseudocapacitors, which can be described as empirical dependencies [45–47]:

$$j = j_{cap} + j_{diff} = a \cdot v^b \tag{4}$$

where v is the scan rate, a and b are adjustable parameters, and parameter b is determined directly by the slope of the $logi$ vs. $logv$. As a rule, if the slope of b is 1, a surface redox

reaction involving processes not controlled by diffusion is expected; at the same time, for an ideal Faraday process controlled by diffusion, the slope of *b* is 0.5 [48,49].
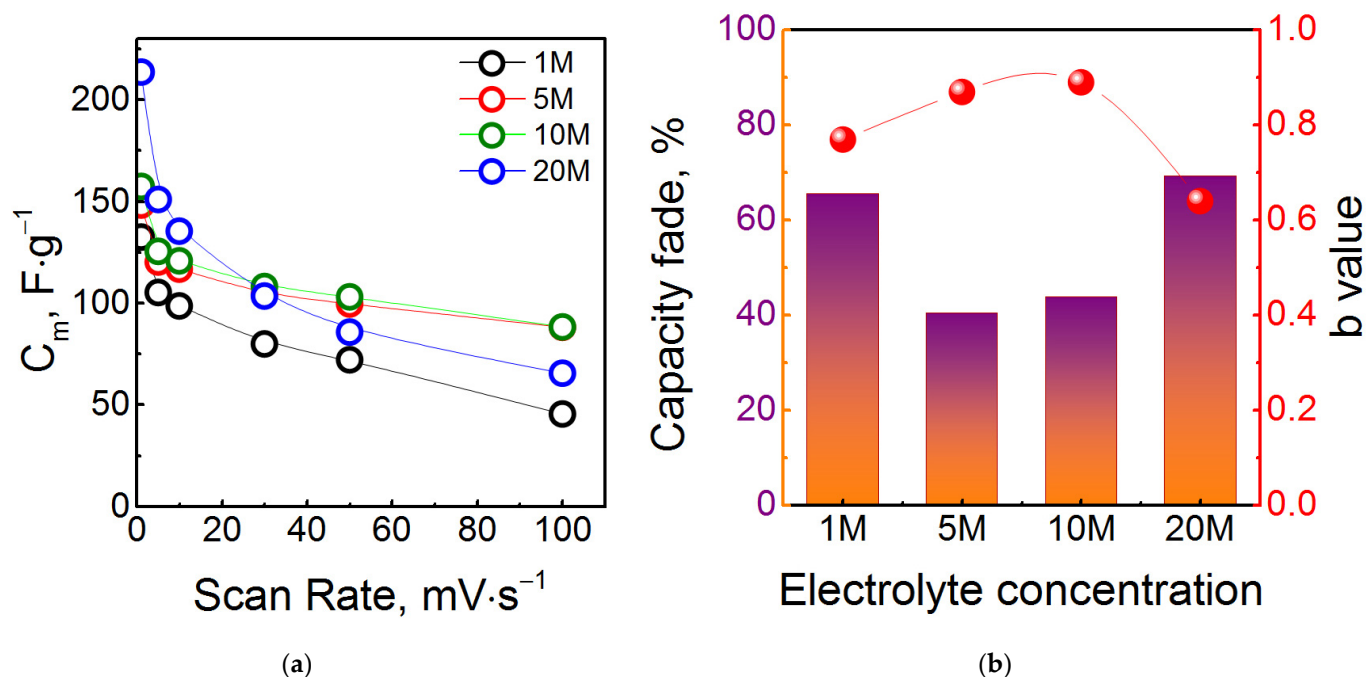

Figure 4. Dependence of the specific capacitance on the scan rate for different electrolyte concentrations (**a**) and the study of the capacitance fade and the determination of the b value depending on the electrolyte concentration (**b**).

As shown in Figure 4b for the $Ti_3C_2T_x$ MXene electrode, the obtained *b* values are in the range of 0.64–0.89 depending on the electrolyte concentration, which indicates the presence of diffusion and surface-capacitive processes. Further quantification of the capacitive and diffusive contributions to the total capacitance is analyzed using the following equation [50–53]:

$$j(U) = j_{cap} + j_{diff} = k \cdot v_1 + k v_2^{0.5} \tag{5}$$

where v is the scan rate, and k_1 and $k_2 v^{0.5}$ represent currents due to the contribution of surface capacitance and diffusion-controlled processes, respectively. The values of k_1 and k_2 can be estimated from the slopes and intersections on the linear plots of $i(U)/v^{0.5}$ vs. $v^{0.5}$, respectively.

As shown in Figure 5, the shaded area corresponds to the contribution of the surface capacitance to the total capacitance of the $Ti_3C_2T_x$ electrode in the 5 M LiCl electrolyte. In this case, the contribution of the surface capacitance to the total capacitance is about 40% and depends little on the scan rate.

Wide peaks are observed on the CV curves, which indicates the presence of pseudocapacity. However, based on the quantitative definition, the diffusion process is predominant. This is not surprising, since MXene also can be considered as electrode materials for energy storage devices capable of reversibly intercalating lithium ions into the structure. The synthesized MXene contains lithium in the structure. The reversible extraction of lithium from the structure of the studied MXene provides an additional contribution to the diffusion process due to the operation of the Ti^{4+}/Ti^{3+} couple. In addition, the redox contribution occurs in MXene from changes in the oxidation degrees of the surface atoms of transition metals. Redox processes are not limited to diffusion and, thus, represent controlled processes of "semi-diffusion" [45].
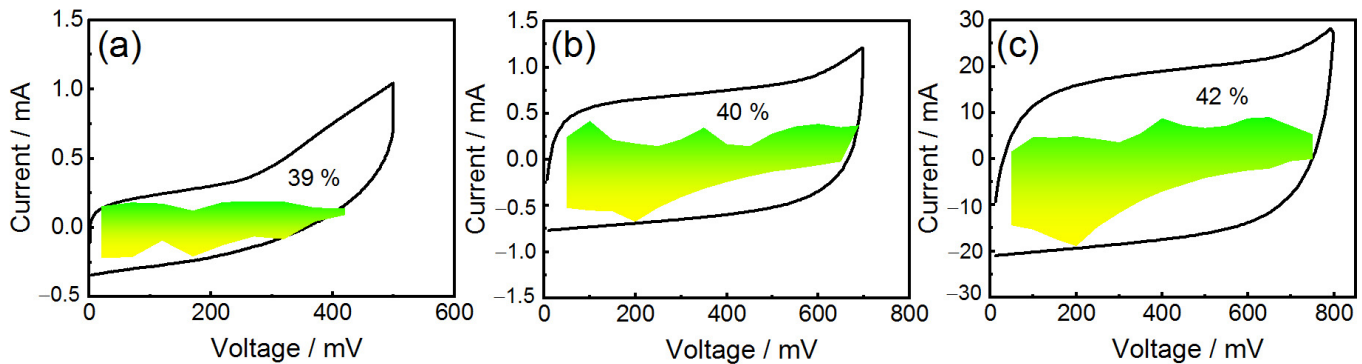
Figure 5. CV partition analysis showing capacitive contribution to total current at (**a**) $1 \text{ mV} \cdot \text{s}^{-1}$, (**b**) $30 \text{ mV} \cdot \text{s}^{-1}$, and (**c**) $100 \text{ mV} \cdot \text{s}^{-1}$.

Galvanostatic charge–discharge curves from 0.25 to $5 \text{ A} \cdot \text{g}^{-1}$ are shown in Figure 6a. As can be seen, the charge–discharge curves show a slight deviation from the triangular curves, which is due to the contribution of the redox reaction of the $Ti_3C_2T_x$ MXene electrodes. The discharge curve has a shape close to an inclined straight line, which indicates the absence of redox transformations of the electrode material. With increasing current density, an increase in the voltage drop IR after charging can be observed. In addition, as shown in Figure 6b, the symmetrical supercapacitor with 5 M electrolyte exhibits good cyclic stability with capacitance retention of 88% over 10,000 cycles, at a galvanostatic charge–discharge at $1 \text{ A} \cdot \text{g}^{-1}$ current density.
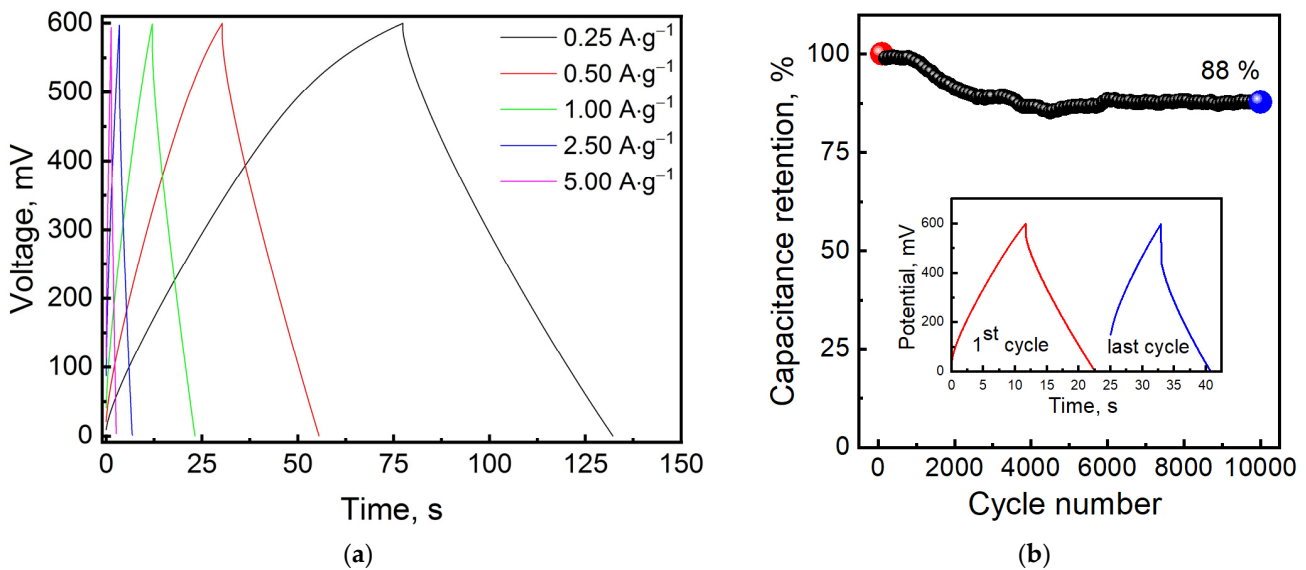

Figure 6. Galvanostatic charge–discharge curves of the symmetrical supercapacitor with 5 M electrolyte and $Ti_3C_2T_x$ MXene electrodes at different current densities (**a**). Cyclic stability of $Ti_3C_2T_x$ MXene over 10,000 cycles at a galvanostatic charge–discharge at $1 \text{ A} \cdot \text{g}^{-1}$ current density (**b**).

The impedance of symmetrical supercapacitors based on MXene consists of the impedance of current collectors, electrolyte, and electrode–electrolyte interfaces. So, the shape of the Nyquist plots for supercapacitors (Figure 7a–f) describes the inherent property of electrode materials in three main segments (high-, medium-, and low-frequency regions). It consists of a semicircle in the high-frequency region and two linear sections in the mid-frequency region, corresponding to the diffusion impedance, and in the low-frequency region for electrochemical capacitance of the electrodes. The equivalent circuit for such supercapacitors consists of series sections: 1. series resistance R_s; 2. parallel connected CPE_{dl} and R_{ct}; 3. Warburg impedance W; 3. CPE_{el} capacitive impedance of the electrodes.

It can be written like this: $R_s + (CPE_{dl}/R_{ct}) + W + CPE_{el}$. The high-frequency region describes a combination of resistances (R_s) consisting of an electrolyte, a separator, and a current collector. The semicircle in the mid-frequency region shows the charge transfer resistance and capacitance of the double layer, i.e., determines the values of the equivalent series resistance (ESR). The mid-frequency sloping region may be related to the diffusion of ions on the electrode surface, which indicates pseudocapacitive behavior. The low-frequency sloping region for all samples has a larger slope angle than the mid-frequency one, which confirms the capacitive processes of the electrodes. The R_s values (Table 1, Figure 7a) for the four tested supercapacitors with LiCl concentrations of 1, 5, 10, and 20 M have a dependence corresponding to the conductivity of the electrolyte solutions. For concentrations of 1 M and 20 M, the resistances are greater than for 5 M and 10 M, which confirms that R_s is mainly associated with electrolyte behavior. A significant change in R_s (Table 2, Figure 7f) at a constant voltage can be associated with a small difference in migrating ions in the electrode–electrolyte boundary layers. There is an increase in the values of the Warburg element with an increase in the electrolyte concentration, which indicates an increase in the proportion of diffusion restrictions on charge accumulation with an increase in the ion concentration. A sample with electrolyte concentration of 5 M has the low-frequency region closest to the vertical angle, which indicates the predominance of capacitive processes in it at the electrode–electrolyte interface. The deviation from the verticality of the low-frequency region for the remaining samples, tending to 45°, indicates poor capacitive characteristics.
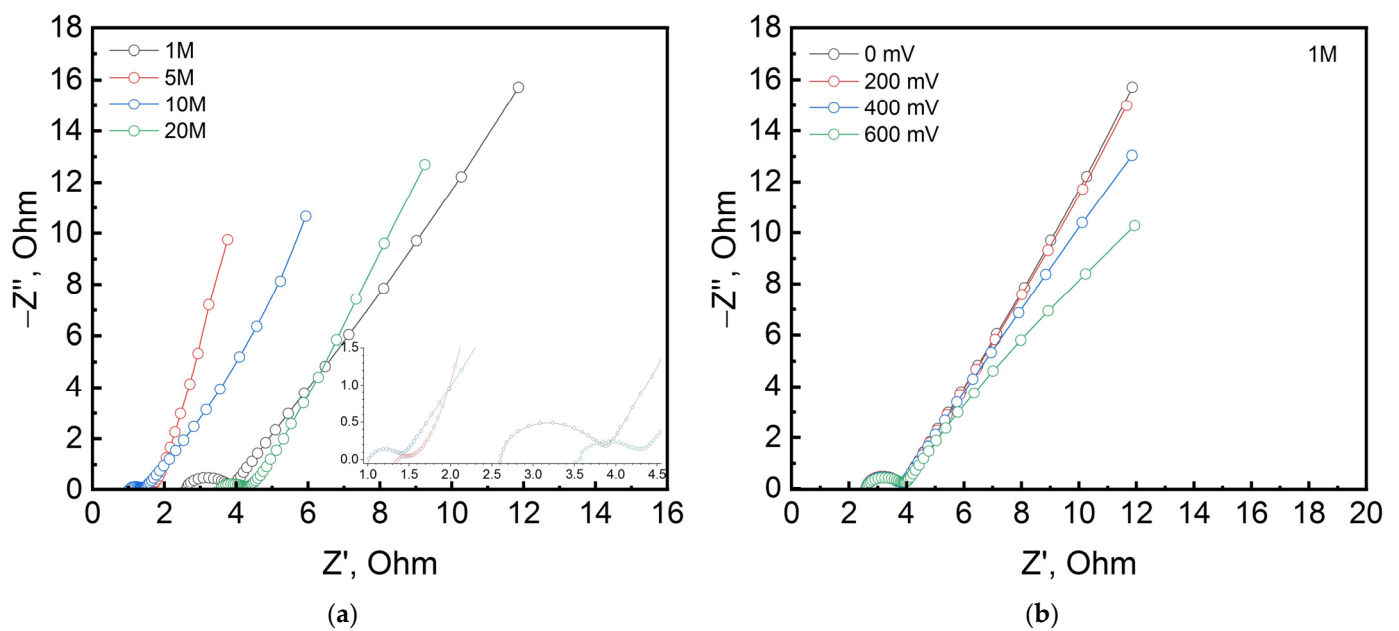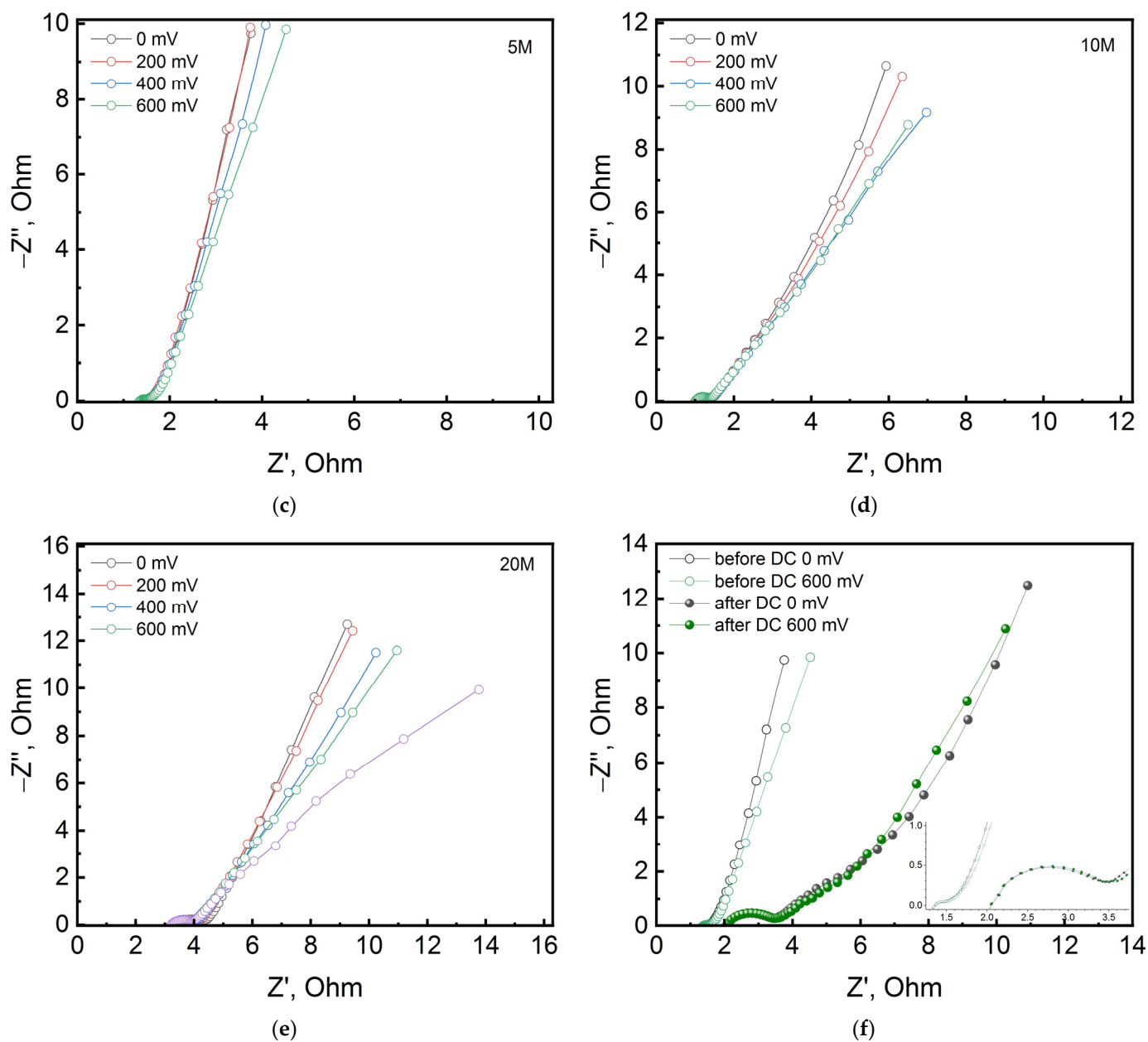

(a)

(b)

Figure 7. *Cont.*

Figure 7. The Nyquist plots for supercapacitors based on MXene: for different electrolyte concentrations and applied voltage: 0 mV (**a**); of DEIS study for electrolyte concentrations 1 M (**b**), 5 M (**c**), 10 M (**d**), and 20 M (**e**); for electrolyte concentration 5 M and applied voltages: 0 mV and 600 mV after and before cycling (**f**).

Table 1. Impedance parameters of supercapacitors based on MXene for different electrolyte concentration.

Electrolyte Concentration	1 M	5 M	5 M after Cycling	10 M	20 M
R_s, Ohm	2.594	1.172	1.918	0.940	3.503
CPE_{dl}, mF·s$^{(a-1)}$	0.1	7.228	191	0.286	0.96
n_{dl}	0.888	0.486	0.750	0.817	0.688
R_{ct}, Ohm	1.19	0.358	1.384	0.423	0.789
W, Ohm·s$^{-1/2}$	1.372	1.530	9.560	2.453	1.964
CPE_{el}, F·s$^{(a-1)}$	0.087	0.191	0.148	0.179	0.136
n_{el}	0.718	1	0.982	0.837	0.851

Table 2. Impedance parameters of supercapacitors based on MXene with electrolyte of 5 M LiCl for different applied voltage.

Applied Voltage, mV	0	200	400	600	600 after Cycling
R_s, Ohm	1.172	1.228	1.325	1.208	1.898
CPE_{dl}, mF·s$^{(a-1)}$	7.228	8.697	2.323	93	0.237
n_{dl}	0.486	0.510	0.730	0.304	0.731
R_{ct}, Ohm	0.358	0.297	0.206	0.481	1.475
W, Ohm·s$^{-1/2}$	1.530	1.480	1.434	0.798	8.245
CPE_{el}, F·s$^{(a-1)}$	0.191	0.186	0.184	0.164	0.128
n_{el}	1	1	0.960	0.883	0.777

Impedance measurements without applied voltage provide limited information on the physicochemical properties of materials and are insufficient to understand the characteristics of electrodes. In addition to conventional electrochemical measurements, this study used an advanced method of dynamic electrochemical impedance spectroscopy (DEIS) [54,55]. Comparative Nyquist plots for supercapacitors based on MXene electrodes with 1, 5, 10, and 20 M LiCl electrolytes obtained using DEIS under charging voltage conditions are shown in Figure 7b–e. At the same time, for electrolyte concentrations of 1, 5, and 10 M, the voltage series was 0 mV, 200 mV, 400 mV, and 600 mV; for 20 M, it is supplemented with a voltage of 800 mV since the potential window for it is about 1000 mV. A capacitive tail with a slope value above 80°, almost parallel to the imaginary axis, exhibits relatively excellent capacitive behavior and only corresponds to the 5 M electrolyte sample. An increase in the applied voltage leads to a decrease in the angle of the low-frequency region of the impedance hodographs.

In Figure 7b–e, the size of the semicircle is determined by the capacitance of the double layer (C_{dl}) and cuts off the value of the charge transfer resistance (R_{ct}) from the real axis. The sum of R_s and R_{ct} increases from the applied voltage for all electrolyte concentrations. In this case, for example, for the 5 M concentration (Table 2), the nonlinear change in R_{ct} can be explained by the inhomogeneous pore structure with no mesoporosity. The typical behavior of an ideal capacitor is an increase in C_{dl} and a decrease in R_{ct} with applied voltage, which clearly shows the electrochemical characteristics of the material, such as capacitance and discharge current density. Thus, a sample with an electrolyte concentration of 5 M exhibits downward behavior at a higher applied voltage for R_{ct}. An increase in the applied voltage decreases the values of the Warburg element.

After cycling the supercapacitor with 5 M electrolyte with 10,000 galvanostatic charge–discharges cycles, a change in the shape of the hodograph (Figure 7f) and the values of the fitted parameters in Table 1 for DC 0 (column 5 M after cycling) and Table 2 column (600 mV after cycling) are observed. Thus, the value of the charge transfer resistance and the Warburg impedance increase significantly, which confirms the degradation of the electrode material. The capacitance values decrease by 14%, which correlates with the value obtained by the galvanostatic charge–discharge method. The results of the DEIS experiments correlate with CV and galvanostatic charge–discharge.

The parameters of SCs' analogs based on layered MXene are presented in Table 3. As can be seen, the cyclic stability of SCs based on multilayer $Ti_3C_2T_x$ and LiCl electrolytes is also at a high level, as in analogs based on layered MXene with $LiPF_6$, H_2SO_4, and $NaClO_4$ electrolytes, which confirms the high reversibility of redox reactions occurring during energy storage. At the same time, the specific capacitance of the studied SCs may exceed some analogues but has lower values compared to layered MXene operating with H_2SO_4 electrolytes. However, LiCl is a safer neutral electrolyte than sulfuric acid, which makes it more attractive for practical applications. In addition, the use of multilayer MXenes is preferred due to their ease of preparation and scale production compared to layered 2D MXenes.

Table 3. Summary of electrochemical performance for MXene electrode materials and electrolyte in supercapacitors.

Electrode Material	Electrolyte	Capacitance, F g^{-1}	Capacitance Retention	Ref.
CTAB-Sn(IV)@Ti$_3$C$_2$//AC	1 M LiPF$_6$ in EC:DEC:EMC (1:1:1 *v:v:v*) + 1 wt.% FEC	51	71.1% (4000 cycles)	[56]
Co(OH)$_2$/Ti$_3$C$_2$T$_x$	5 M LiCl	153	99.0% (1000 cycles)	[57]
Bistacked 2D titanium carbide	Non-aqueous 1 M NaClO$_4$	104	84.2% (4000 cycles)	[58]
Ta$_4$C$_3$	0.1 M H$_2$SO$_4$	120	89.0% (2000 cycles)	[59]
EDA-Ti$_3$C$_2$T$_x$	3 M H$_2$SO$_4$	249.4	89.7% (10,000 cycles)	[60]
Ti$_2$CT$_x$/OLS(5%)	1 M H$_2$SO$_4$	102.03	100% (10,000 cycles)	[61]
Multilayered Ti$_3$C$_2$T$_x$	5 M LiCl	120	88% (10,000 cycles)	This work

4. Conclusions

Ti$_3$C$_2$T$_x$ MXene powder was successfully synthesized as a result of selective etching of an Al layer from Ti$_3$AlC$_2$ MAX phase by hydrothermal treating in a mixture of HCl and LiF. The obtained MXenes were studied as the active electrode material of a supercapacitor, which additionally included carbon black and poly(vinylidene fluoride) at a mass ratio of Ti$_3$C$_2$T$_x$/CB/PVDF = 8/1/1. Its electrochemical studies were carried out in assembled symmetrical coin cell using aqueous solutions of LiCl with concentrations of 1, 5, 10, and 20 M. At a scan rate of 5 mV·s^{-1}, for SCs with electrolyte concentrations of 1, 5, 10, and 20 M, the specific capacitances are 105, 120, 126, and 151 F·g^{-1}, respectively. The value of the parameter b from empirical dependency for capacitors found graphically was in the range 0.64–0.89 depending on the electrolyte concentration, which indicates the presence of diffusion and surface-capacitive processes. The contribution of the surface capacitance to the total capacitance of studied SCs with Ti$_3$C$_2$T$_x$ MXene electrodes was about 40% and depends little on the scan rate. In addition, Ti$_3$C$_2$T$_x$ electrodes showed high redox reversibility and good cyclic stability with capacitance retention of 88% over 10,000 cycles. A relationship has been found between the parameters of the impedance equivalent circuit with changes in the electrolyte concentration, the applied constant voltage, and their degradation after cycling with 10,000 cycles of galvanostatic charge–discharge for a sample with an electrolyte concentration of 5 M.

Author Contributions: Conceptualization, A.T., A.S. and N.G.; methodology, A.T. and D.Z.; software, A.S. and N.G.; validation, N.G. and M.V.; formal analysis, M.V., A.T., N.G. and A.G.; investigation, A.T., A.S. and N.G.; data curation, A.S., D.Z. and N.G.; writing—original draft preparation, A.T., A.S. and M.V.; writing—review and editing, A.G. and N.G.; visualization, M.V. and N.G.; supervision, A.G. and N.G.; project administration, N.G.; funding acquisition, N.G. All authors have read and agreed to the published version of the manuscript.

Data Availability Statement: Not applicable.

Conflicts of Interest: The authors declare no conflict of interest.

References

1. Collath, N.; Tepe, B.; Englberger, S.; Jossen, A.; Hesse, H. Aging aware operation of lithium-ion battery energy storage systems: A review. *J. Energy Storage* **2022**, *55*, 105634. [CrossRef]
2. Arico, A.S.; Bruce, P.; Scrosati, B.; Tarascon, J.M.; Van Schalkwijk, W. Nanostructured materials for advanced energy conversion and storage devices. *Nat. Mater.* **2005**, *4*, 366–377. [CrossRef] [PubMed]

3. Deng, W.N.; Li, Y.H.; Xu, D.F.; Zhou, W.; Xiang, K.X.; Chen, H. Three-dimensional hierarchically porous nitrogen-doped carbon from water hyacinth as selenium host for high-performance lithium–selenium batteries. *Rare Met.* **2022**, *41*, 3432–3445. [CrossRef]

4. Hwang, J.Y.; Myung, S.T.; Sun, Y.K. Sodium-ion batteries: Present and future. *Chem. Soc. Rev.* **2017**, *46*, 3529–3614. [PubMed]

5. Deng, W.; Xu, Y.; Zhang, X.; Li, C.; Liu, Y.; Xiang, K.; Chen, H. $(NH_4)_2Co_2V_{10}O_{28}\cdot 16H_2O/(NH_4)_2V_{10}O_{25}\cdot 8H_2O$ heterostructure as cathode for high-performance aqueous Zn-ion batteries. *J. Alloys Compd.* **2022**, *903*, 163824. [CrossRef]

6. Zhou, W.; Zeng, G.; Jin, H.; Jiang, S.; Huang, M.; Zhang, C.; Chen, H. Bio-Template Synthesis of V_2O_3@Carbonized Dictyophora Composites for Advanced Aqueous Zinc-Ion Batteries. *Molecules* **2023**, *28*, 2147. [CrossRef]

7. Wen, X.; Luo, J.; Xiang, K.; Zhou, W.; Zhang, C.; Chen, H. High-performance monoclinic WO_3 nanospheres with the novel NH^{4+} diffusion behaviors for aqueous ammonium-ion batteries. *Chem. Eng. J.* **2023**, *458*, 141381. [CrossRef]

8. Xiao, J.; Li, H.; Zhang, H.; He, S.; Zhang, Q.; Liu, K.; Jiang, S.; Duan, G.; Zhang, K. Nanocellulose and its derived composite electrodes toward supercapacitors: Fabrication, properties, and challenges. *J. Bioresour. Bioprod.* **2022**, *7*, 245–269.

9. Dar, M.A.; Dinagaran, S.; Govindarajan, D.; Ahamed, S.R.; Habib, F.; Siva, C.; Moholkar, A.V.; Ahmad, Z.; Yatoo, M.A. $Sn_{x-0}Mn_xS$ nanomaterial based electrodes for future-generation supercapacitor and data storage devices. *J. Alloys Compd.* **2023**, *958*, 170523. [CrossRef]

10. Simon, P.; Gogotsi, Y. Materials for electrochemical capacitors. *Nat. Mater.* **2008**, *7*, 845–854. [CrossRef]

11. Raza, W.; Ali, F.; Raza, N.; Luo, Y.; Kim, K.H.; Yang, J.; Kumar, S.; Mehmood, A.; Kwon, E.E. Recent advancements in supercapacitor technology. *Nano Energy* **2018**, *52*, 441–473. [CrossRef]

12. Saikia, B.K.; Benoy, S.M.; Bora, M.; Tamuly, J.; Pandey, M.; Bhattacharya, D. A brief review on supercapacitor energy storage devices and utilization of natural carbon resources as their electrode materials. *Fuel* **2020**, *282*, 118796. [CrossRef]

13. Liu, S.; Sun, S.; You, X.Z. Inorganic nanostructured materials for high performance electrochemical supercapacitors. *Nanoscale* **2014**, *6*, 2037–2045. [CrossRef] [PubMed]

14. Baboo, J.P.; Jakubczyk, E.; Yatoo, M.A.; Phillips, M.; Grabe, S.; Dent, M.; Hinder, S.J.; Watts, J.F.; Lekakou, C. Investigating battery-supercapacitor material hybrid configurations in energy storage device cycling at 0.1 to 10C rate. *J. Power Sources* **2023**, *561*, 232762. [CrossRef]

15. Zhu, X. Recent advances of transition metal oxides and chalcogenides in pseudo-capacitors and hybrid capacitors: A review of structures, synthetic strategies, and mechanism studies. *J. Energy Storage* **2022**, *49*, 104148. [CrossRef]

16. Bhojane, P. Recent advances and fundamentals of Pseudocapacitors: Materials, mechanism, and its understanding. *J. Energy Storage* **2022**, *45*, 103654. [CrossRef]

17. Zhang, Y.; Yan, Y.; Qiu, H.; Ma, Z.; Ruan, K.; Gu, J. A mini-review of MXene porous films: Preparation, mechanism and application. *J. Mater. Sci. Technol.* **2022**, *103*, 42–49. [CrossRef]

18. Yan, J.; Li, S.; Lan, B.; Wu, Y.; Lee, P.S. Rational design of nanostructured electrode materials toward multifunctional supercapacitors. *Adv. Funct. Mater.* **2020**, *30*, 1902564. [CrossRef]

19. Arbi, H.M.; Vijayalakshmi, L.; Anil Kumar, Y.; Alzahmi, S.; Gopi, C.V.V.M.; Rusydi, A.; Obaidat, I.M. A Facile Two-Step Hydrothermal Synthesis of $Co(OH)_2$@$NiCo_2O_4$ Nanosheet Nanocomposites for Supercapacitor Electrodes. *Nanomaterials* **2023**, *13*, 1981. [CrossRef]

20. Kumar, S.; Ahmed, F.; Shaalan, N.M.; Arshi, N.; Dalela, S.; Chae, K.H. Investigations of Structural, Magnetic, and Electrochemical Properties of $NiFe_2O_4$ Nanoparticles as Electrode Materials for Supercapacitor Applications. *Materials* **2023**, *16*, 4328. [CrossRef]

21. Senthil, R.A.; Min, A.; Theerthagiri, J.; Kim, G.A.; Choi, H.C.; Choi, M.Y. Insights on Ni-based layered double hydroxides for electrochemical supercapacitors: Underlying aspects in rational design and structural evolution. *J. Energy Storage* **2023**, *72*, 108305. [CrossRef]

22. Kandasamy, M.; Sahoo, S.; Nayak, S.K.; Chakraborty, B.; Rout, C.S. Recent advances in engineered metal oxide nanostructures for supercapacitor applications: Experimental and theoretical aspects. *J. Mater. Chem. A* **2021**, *9*, 17643–17700. [CrossRef]

23. Bokhari, S.W.; Siddique, A.H.; Sherrell, P.C.; Yue, X.; Karumbaiah, K.M.; Wei, S.; Ellis, A.V.; Gao, W. Advances in graphene-based supercapacitor electrodes. *Energy Rep.* **2020**, *6*, 2768–2784. [CrossRef]

24. Li, Q.; Li, Y.; Zeng, W. Preparation and Application of 2D MXene-Based Gas Sensors: A Review. *Chemosensors* **2021**, *9*, 225. [CrossRef]

25. Perera, A.A.P.R.; Madhushani, K.A.U.; Punchihewa, B.T.; Kumar, A.; Gupta, R.K. MXene-Based Nanomaterials for Multifunctional Applications. *Materials* **2023**, *16*, 1138. [CrossRef]

26. Liu, J.; Chen, S.; He, J.; Huang, R.; Tao, L.; Zhao, Y.; Yang, Y. $Ti_3C_2T_x$ MXene Quantum Dots with Surface-Terminated Groups (–F, –OH, =O, –Cl) for Ultrafast Photonics. *Nanomaterials* **2022**, *12*, 2043. [CrossRef]

27. Tsyganov, A.; Vikulova, M.; Artyukhov, D.; Zheleznov, D.; Gorokhovsky, A.; Gorshkov, N. Intercalation Effects on the Dielectric Properties of PVDF/$Ti_3C_2T_x$ MXene Nanocomposites. *Nanomaterials* **2023**, *13*, 1337. [CrossRef]

28. Tseluikin, V.; Dzhumieva, A.; Tribis, A.; Tikhonov, D.; Tsyganov, A.; Gorshkov, N.; Lopukhova, M. Study of Electrodeposition and Properties of Composite Nickel Coatings Modified with $Ti_3C_2T_X$ MXene. *Coatings* **2023**, *13*, 1042. [CrossRef]

29. Raja Sulaiman, R.R.; Hanan, A.; Wong, W.Y.; Mohamad Yunus, R.; Shyuan Loh, K.; Walvekar, R.; Chaudhary, V.; Khalid, M. Structurally Modified MXenes-Based Catalysts for Application in Hydrogen Evolution Reaction: A Review. *Catalysts* **2022**, *12*, 1576. [CrossRef]

30. Murali, G.; Reddy Modigunta, J.K.; Park, Y.H.; Lee, J.H.; Rawal, J.; Lee, S.Y.; In, I.; Park, S.J. A review on MXene synthesis, stability, and photocatalytic applications. *ACS Nano* **2022**, *16*, 13370–13429. [CrossRef]

31. Arumugam, B.; Mayakrishnan, G.; Subburayan Manickavasagam, S.K.; Kim, S.C.; Vanaraj, R. An Overview of Active Electrode Materials for the Efficient High-Performance Supercapacitor Application. *Crystals* **2023**, *13*, 1118. [CrossRef]
32. Liang, W.; Xu, R.; Nawwar, M.; Zhitomirsky, I. Multifunctional MXene–Fe_3O_4–Carbon Nanotube Composite Electrodes for High Active Mass Asymmetric Supercapacitors. *Batteries* **2023**, *9*, 327. [CrossRef]
33. Guan, G.; Guo, F. A Review of Nb_2CT_x MXene: Synthesis, Properties and Applications. *Batteries* **2023**, *9*, 235. [CrossRef]
34. Forouzandeh, P.; Pillai, S.C. MXenes-based nanocomposites for supercapacitor applications. *Curr. Opin. Chem. Eng.* **2021**, *33*, 100710. [CrossRef]
35. Zhang, A.; Liu, R.; Tian, J.; Huang, W.; Liu, J. MXene-based nanocomposites for energy conversion and storage applications. *Chem. Eur. J.* **2020**, *26*, 6342–6359. [CrossRef]
36. Huang, Y.; Lu, Q.; Wu, D.; Jiang, Y.; Liu, Z.; Chen, B.; Zhu, M.; Schmidt, O.G. Flexible MXene films for batteries and beyond. *Carbon Energy* **2022**, *4*, 598–620. [CrossRef]
37. Wang, J.; He, J.; Kan, D.; Chen, K.; Song, M.; Huo, W. MXene Film Prepared by Vacuum-Assisted Filtration: Properties and Applications. *Crystals* **2022**, *12*, 1034. [CrossRef]
38. Xi, W.; Zhang, Y.; Zhang, J.; Wang, R.; Gong, Y.; He, B.; Wang, H.; Jin, J. Constructing MXene hydrogels and aerogels for rechargeable supercapacitors and batteries. *J. Mater. Chem. C* **2023**, *11*, 2414–2429. [CrossRef]
39. Li, K.; Li, J.; Zhu, Q.; Xu, B. Three-dimensional MXenes for supercapacitors: A review. *Small Methods* **2022**, *6*, 2101537. [CrossRef]
40. Hu, M.; Li, Z.; Hu, T.; Zhu, S.; Zhang, C.; Wang, X. High-capacitance mechanism for $Ti_3C_2T_x$ MXene by in situ electrochemical raman spectroscopy investigation. *ACS Nano* **2016**, *10*, 11344–11350. [CrossRef]
41. Fu, J.; Li, L.; Lee, D.; Yun, J.M.; Ryu, B.K.; Kim, K.H. Enhanced electrochemical performance of $Ti_3C_2T_x$ MXene film based supercapacitors in H_2SO_4/KI redox additive electrolyte. *Appl. Surf. Sci.* **2020**, *504*, 144250. [CrossRef]
42. Wang, L.; Liu, D.; Lian, W.; Hu, Q.; Liu, X.; Zhou, A. The preparation of V_2CT_x by facile hydrothermal-assisted etching processing and its performance in lithium-ion battery. *J. Mater. Res. Technol.* **2020**, *9*, 984–993. [CrossRef]
43. Ghosh, A.; Pal, H.; Das, T.; Chatterjee, S.; Das, A. Synthesis and Characterization of MXene from MAX phase. *Mater. Today Proc.* **2022**, *58*, 714–716. [CrossRef]
44. Jiang, Q.; Kurra, N.; Alhabeb, M.; Gogotsi, Y.; Alshareef, H.N. All pseudocapacitive MXene-RuO_2 asymmetric supercapacitors. *Adv. Energy Mater.* **2018**, *8*, 1703043. [CrossRef]
45. Tao, Q.; Dahlqvist, M.; Lu, J.; Kota, S.; Meshkian, R.; Halim, J.; Palisaitis, J.; Hultman, L.; Barsoum, M.W.; Persson, P.O.A.; et al. Two-dimensional $Mo_{1.33}C$ MXene with divacancy ordering prepared from parent 3D laminate with in-plane chemical ordering. *Nat. Commun.* **2017**, *8*, 14949. [CrossRef]
46. MacArthur, D.M. The hydrated nickel hydroxide electrode potential sweep experiments. *J. Electrochem. Soc.* **1970**, *117*, 422–426. [CrossRef]
47. Kim, H.S.; Cook, J.B.; Lin, H.; Ko, J.S.; Tolbert, S.H.; Ozolins, V.; Dunn, B. Oxygen vacancies enhance pseudocapacitive charge storage properties of $MoO_{3−x}$. *Nat. Mater.* **2017**, *16*, 454–460. [CrossRef]
48. Liu, J.; Wang, J.; Xu, C.; Jiang, H.; Li, C.; Zhang, L.; Lin, J.; Shen, Z.X. Advanced energy storage devices: Basic principles, analytical methods, and rational materials design. *Adv. Sci.* **2018**, *5*, 1700322. [CrossRef]
49. Chao, D.; Liang, P.; Chen, Z.; Bai, L.; Shen, H.; Liu, X.; Xia, X.; Zhao, Y.; Savilov, S.V.; Lin, J.; et al. Pseudocapacitive Na-ion storage boosts high rate and areal capacity of self-branched 2D layered metal chalcogenide nanoarrays. *ACS Nano* **2016**, *10*, 10211–10219. [CrossRef]
50. Ghidiu, M.; Lukatskaya, M.R.; Zhao, M.Q.; Gogotsi, Y.; Barsoum, M.W. Conductive two-dimensional titanium carbide 'clay' with high volumetric capacitance. *Nature* **2014**, *516*, 78–81. [CrossRef]
51. Wang, J.; Polleux, J.; Lim, J.; Dunn, B. Pseudocapacitive contributions to electrochemical energy storage in TiO_2 (anatase) nanoparticles. *J. Phys. Chem. C* **2007**, *111*, 14925–14931. [CrossRef]
52. Brezesinski, T.; Wang, J.; Tolbert, S.H.; Dunn, B. Ordered mesoporous α-MoO_3 with iso-oriented nanocrystalline walls for thin-film pseudocapacitors. *Nat. Mater.* **2010**, *9*, 146–151. [CrossRef] [PubMed]
53. Chao, D.; Zhu, C.; Yang, P.; Xia, X.; Liu, J.; Wang, J.; Fan, X.; Savilov, S.V.; Lin, J.; Fan, H.J.; et al. Array of nanosheets render ultrafast and high-capacity Na-ion storage by tunable pseudocapacitance. *Nat. Commun.* **2016**, *7*, 12122. [CrossRef] [PubMed]
54. Ramesh, T.; Vedarajan, R.; Rajalakshmi, N.; Reddy, L.R. Dynamic electrochemical impedance spectroscopy as a rapid screening tool for supercapacitor electrode materials. *J. Mater. Sci. Mater. Electron.* **2020**, *31*, 1681–1690. [CrossRef]
55. Wang, S.; Zhang, J.; Gharbi, O.; Vivier, V.; Gao, M.; Orazem, M.E. Electrochemical impedance spectroscopy. *Nat. Rev. Methods Primers* **2021**, *1*, 41. [CrossRef]
56. Luo, J.; Zhang, W.; Yuan, H.; Jin, C.; Zhang, L.; Huang, H.; Liang, C.; Xia, Y.; Zhang, J.; Gan, Y.; et al. Pillared Structure Design of MXene with Ultralarge Interlayer Spacing for High-Performance Lithium-Ion Capacitors. *ACS Nano* **2017**, *11*, 2459–2469. [CrossRef]
57. Jiang, H.; Wang, Z.; Dong, L.; Dong, M. $Co(OH)_2$/MXene composites for tunable pseudo-capacitance energy storage. *Electrochim. Acta* **2020**, *353*, 136607. [CrossRef]
58. Kurra, N.; Alhabeb, M.; Maleski, K.; Wang, C.H.; Alshareef, H.N.; Gogotsi, Y. Bistacked titanium carbide (MXene) anodes for hybrid sodium-ion capacitors. *ACS Energy Lett.* **2018**, *3*, 2094–2100. [CrossRef]
59. Syamsai, R.; Grace, A.N. Ta_4C_3 MXene as supercapacitor electrodes. *J. Alloys Compd.* **2019**, *792*, 1230–1238. [CrossRef]

60. Xu, P.; Xiao, H.; Liang, X.; Zhang, T.; Zhang, F.; Liu, C.; Lang, B.; Gao, Q. A MXene-based EDA-Ti$_3$C$_2$T$_x$ intercalation compound with expanded interlayer spacing as high performance supercapacitor electrode material. *Carbon* **2021**, *173*, 135–144. [CrossRef]
61. Habib, I.; Ferrer, P.; Ray, S.C.; Ozoemena, K.I. Interrogating the impact of onion-like carbons on the supercapacitive properties of MXene (Ti$_2$CT$_X$). *J. Appl. Phys.* **2019**, *126*, 134301. [CrossRef]